# Iron-rich Silicates in the Earth's D" Layer

Wendy L. Mao[1,2], Yue Meng[3], Guoyin Shen[4], Vitali B. Prakapenka[4], Andrew J. Campbell[1,5], Dion L. Heinz[1,6], Jinfu Shu[2], Razvan Caracas[2], Ronald E. Cohen[2], Yingwei Fei[2], Russell J. Hemley[2], and Ho-kwang Mao[1,2,3,6]

[1]*Department of the Geophysical Sciences, University of Chicago, Chicago, IL 60637*

[2]*Geophysical Laboratory, Carnegie Institution of Washington, Washington, D.C. 20015*

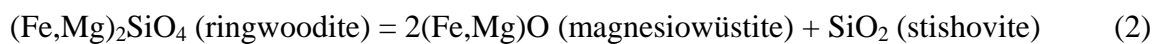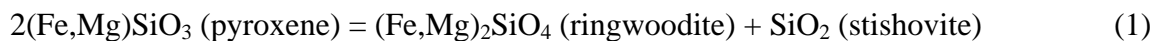[3]*HPCAT, Advanced Photon Source, Argonne National Laboratory, Argonne, IL 60439*

[4]*Consortium for Advanced Radiation Sources, University of Chicago, Chicago, IL 60637*

[5]*Chicago Center for Cosmochemistry, University of Chicago, Chicago, IL 60637*

[6]*James Franck Institute, University of Chicago, Chicago, IL 60637*

High-pressure experiments and theoretical calculations demonstrate that an iron-rich ferromagnesian silicate phase can be synthesized at the pressure-temperature conditions near the core-mantle boundary (CMB). This phase is up to 20% denser than any known silicate at CMB. The high mean atomic number of the iron-rich silicate greatly reduces the seismic velocity, and provides a new explanation to the low velocity and ultra low velocity zones. Formation of this phase from reaction between the silicate mantle and the iron core may be responsible for the unusual geophysical and geochemical signatures observed at the base of the lower mantle.

Modern deep-Earth mineralogical research began with high-pressure experiments on iron silicate, a major component in the solid Earth. The discovery of the fayalite ($Fe_2SiO_4$) olivine-spinel transition in 1959 (*1*) marked the first known transition beyond the upper mantle. The disproportionation of fayalite spinel into mixed oxides by using the newly invented laser-heated and resistive-heated diamond-anvil cell in early 1970's (*2, 3*) marked the first phase transition under lower mantle conditions. In the Earth's crust, upper mantle, and transition zone, iron silicates form extensive solid solutions with the magnesium endmembers in major rock-forming minerals, *e.g.*, fayalite in $\alpha$-$(Fe,Mg)_2SiO_4$ (olivine), ferrosilite in $(Fe,Mg)SiO_3$ (pyroxene), almandine in $(Fe,Mg)_3Al_2Si_3O_{12}$ (garnet), and fayalite spinel in $\gamma$-$(Fe,Mg)_2SiO_4$ (ringwoodite). No iron-rich silicate, however, was known to exist under the high pressure-temperature (*P-T*) conditions beyond the 670-km discontinuity that accounts for approximately three quarters of the Earth's total silicates and oxides. Following Birch's 1952 postulation (*4*), iron-rich silicates break down to mixed oxides in the lower mantle.

$$2(Fe,Mg)SiO_3 \text{ (pyroxene)} = (Fe,Mg)_2SiO_4 \text{ (ringwoodite)} + SiO_2 \text{ (stishovite)} \qquad (1)$$

$$(Fe,Mg)_2SiO_4 \text{ (ringwoodite)} = 2(Fe,Mg)O \text{ (magnesiowüstite)} + SiO_2 \text{ (stishovite)} \qquad (2)$$

In the lower-mantle silicate, $(Fe_xMg_{1-x})SiO_3$ perovskite, iron can only participates as a minor component with $x < 0.15$ (*5*), even at the CMB with an unlimited supply of iron from the core. Without a stable iron-rich silicate phase, previous explanations of the complex geochemical and geophysical signatures of the D" layer have been limited to heterogeneous, solid/melt mixtures of iron-poor silicates and iron-rich metals and oxides (*6, 7*).

Recently, Murakami et al. (*8*) reported that pure $MgSiO_3$ transformed from the perovskite structure to the $CaIrO_3$ structure under the *P-T* conditions of the D" layer (see also (*9-11*)). This post-perovskite (ppv) phase was also observed to coexist with silicate perovskite and

magnesiowüstite in experiments with orthopyroxene and olivine starting materials with $x$ up to 0.4, but the Fe content in this phase is undefined due to the unknown Fe/Mg distributions among multiple coexisting ferromagnesian phases(*12*). Here we report experimental and theoretical investigations across the ferrosilite ($FeSiO_3$) – enstatite ($MgSiO_3$) join. We found that iron-rich ($Fe_xMg_{1-x}$)$SiO_3$ with $x$ as high as 0.8 formed a single-phase ppv silicate rather than mixed oxides at the pressures of the D" layer (~130 GPa).

Five orthopyroxene samples with $x$ = 0.2, 0.4, 0.6, 0.8, and 1.0 (denoted Fs20, Fs40, Fs60, Fs80, and Fs100, respectively) were synthesized in a piston-cylinder apparatus. The starting oxide mixtures were prepared by weighing MgO, $Fe_2O_3$ and $SiO_2$, in pyroxene stoichiometry with different iron contents, followed by grinding under acetone in an agate mortar. The oxide mixtures were then placed in a $CO_2$-CO gas-mixing furnace at a temperature of 1473 K and oxygen fugacity ($fO_2$) of $10^{-10.5}$ for 24 hours to reduce all $Fe^{3+}$ to $Fe^{2+}$. The treated mixtures were reground and sealed in gold capsules, which were then compressed in the piston-cylinder apparatus for 48 hours at 1273 K and 1.2 GPa. The product was confirmed by x-ray diffraction as a single phase orthopyroxene.

We compressed Fs20, Fs40, Fs60, Fs80, and Fs100 samples to 120-150 GPa in symmetrical diamond-anvil cells. Beveled diamond anvils with flat culet diameter of 90-100 µm were used to generate the pressure, and rhenium gaskets with laser drilled hole diameters of 35-50 µm were used to confine the samples. Multiple sample configurations: with or without Pt black as a laser absorber, with or without NaCl thermal insulation layers, and with or without additional Au and Pt as pressure markers, were used to optimize the synthesis conditions and to distinguish overlapping diffraction peaks. Rhenium at the sample-gasket interface was also used as a secondary pressure marker (*13*). Double-side YLF laser systems at 13ID-D and 16ID-B

stations of the Advanced Photon Source were used for heating, and monochromatic x-ray beams of $\lambda$ = 0.3344, 0.3888, 0.4008, and 0.4233 Å were used for x-ray diffraction.  The primary x-ray beam was focused down to 5-10 µm through a diamond anvil and impinged on the samples. Diffraction rings up to $2\theta$ = 21° exited through the second diamond anvil and cubic BN seat and were recorded on a CCD  detector for *in-situ* measurements at simultaneous high *P-T* conditions or an image-plate  detector for temperature-quenched sample at high pressures. The diffraction patterns were processed and analyzed with Fit2d software (*14*).

X-ray diffraction at low pressures showed well-crystallized orthopyroxene patterns. Above 20-30 GPa, sharp diffraction rings disappeared and were replaced by a broad background, indicating pressure-induced amorphization of the silicate crystals.  Laser-heating of Fs40 and Fs60 at 30-100 GPa produced assemblages of silicate perovskite, magnesiowüstite, and stishovite. Heating samples compressed directly to 120-150 GPa at 2000 K, Fs20, Fs40, Fs60, and Fs80 transformed to the ppv without a trace of silicate perovskite or mixed oxides (Fig. 1) while the Fs100 sample still produced mixed oxides. All characteristic lines of ppv, including the most intense 022 peak, the 023-131 doublet, and the 132-113-004 triplet, are present in the iron-bearing silicates. Indexing of the peaks and fitting to the ppv *Cmcm* orthorhombic unit cell are listed in Table 1.

With first-principles calculations, we confirmed that indeed iron-rich (Fe,Mg)SiO$_3$ is stabilized in the ppv rather than silicate perovskite structure at CMB.  Spin-polarized calculations were performed using the generalized gradient approximation (GGA) (*15*) of density functional theory (*16, 17*) as implemented in the code ABINIT (*18*). We use Troullier-Martins-type pseudopotentials, generated with the fhi98pp code (*19*). The core electronic configuration is [Ar], [Ne], [Ne] and [He] for Fe, Mg, Si and O respectively. We use a 38 Hartree (1 Ha = 27.2116 eV)

kinetic energy cut-off. The calculations are performed on 4x4x4 and 6x6x4 grids of special $k$ points (20) for silicate perovskite and ppv phases respectively. Convergence tests showed a precision in energy better than 1 mHa/molecule and in pressure of about 1 GPa. We computed the enthalpy of silicate ppv referencing to silicate perovskite (the zero horizontal line) for three compositions: $MgSiO_3$, $Mg_{0.5}Fe_{0.5}SiO_3$, and $FeSiO_3$ (Fig. 2). For ppv enthalpies above zero, silicate perovskite is stable, and below zero, ppv is stable. The silicate perovskite-ppv transition pressure occurs at approximately 113 GPa for $MgSiO_3$, and 63 GPa for $x = 0.5$, and the ppv phase is stable at all pressures with respect to silicate perovskite for the pure $FeSiO_3$ end-member, (Fig. 2). The difference in enthalpy between the ferro- and anti-ferromagnetic configurations for ppv-$FeSiO_3$ is less than 23 meV/formula unit (f.u.) at pressures below 90 GPa (specific volume above 34.6 $\text{Å}^3$/f.u.), which increases with pressure to about 40 meV/f.u. at 150 GPa (specific volume about 31.6 $\text{Å}^3$/f.u.).

With atoms in close-packed configurations, densities of D" minerals essentially depend upon the amount of iron which stands out as the predominant heavy element. In Fig. 3, we plot experimental results of unit-cell volumes and densities of Fs20, Fs40, Fs60, and Fs80 (normalized to 130 GPa) for comparison and evaluation of the effects of iron content. Unlike the lower-pressure ferromagnesian silicates for which the volume increases substantially with increasing iron contents due to the large size of the $Fe^{2+}$ ion in comparison to $Mg^{2+}$, (*e. g.*, $\partial lnV/\partial x = 0.04$ for the silicate perovskite phase (21)), the volume dependence for ppv is small ($\partial lnV/\partial x = 0.02$), possibly indicating $Fe^{2+}$ ion in the compact, low-spin state (22-24). The density of the ppv increases sharply with increasing iron content ($\partial ln\rho/\partial x = 0.30$). While the densities of other lower mantle silicates, including ferromagnesian silicate perovskite and $CaCl_2$-type and $\alpha$-$PbO_2$-type $SiO_2$ (8), cluster around 5.6 gm/cm$^3$ ($\pm 2\%$), the density of the Fe-rich ppv silicate

increases by as much as 20% depending upon the iron content.  Such high density in silicate would have a major impact on the seismic and geodynamic properties of the D" layer. For a first approximation, seismic velocities are reduced inversely proportional to the square root of the increasing density due to the iron enrichment. For instance, a ppv silicate with $x = 0.66$ would be sufficient to lower seismic velocities by 10% as observed in ULVZ.

The vast reservoirs of iron and silicates at the core-mantle boundary provides favorable chemical-physical conditions for the formation of iron-rich ppv silicate which holds the key to understanding the geophysical and geochemical properties of the D" layer (*6, 25-27*). Contrary to the previous thinking that the mantle composition was essentially unchanged by contact with the core – *i.e.*, the composition of the mantle silicate remains within its iron-poor solubility limit of x < 0.15 – the new scenario calls for a reaction layer of denser silicates with much higher iron content. In regions of downward or horizontal movement at the CMB, the thickness of the iron-rich layer is limited by solid reaction and diffusivity.  In upwelling regions, the iron-rich layer is too heavy to rise, and will be pile up under plumes (Fig. 4), resulting in the observed low velocity zones (LVZ) (e.g., under Africa) and ultra low velocity zones (ULVZ) (e.g., under Hawaii) (*28*). Comprehensive studies of the equation of state, elastic anisotropy, diffusivity, rheology, magnetism, and reversible phase relation of ppv as a function of temperature and iron concentration are needed for developing the new paradigm for this most enigmatic layer in the solid Earth (*29, 30*).

**References**

1.      A. E. Ringwood, *Amer. Mineral.* **44**, 659-661 (1959).

2.      H. K. Mao, P. M. Bell, *Carnegie Inst. Washington Yearb.* **70**, 176-178 (1971).

3.      W. A. Bassett, L. C. Ming, *Phys. Earth Planet. Interiors* **6**, 154-160 (1972).

4.      F. Birch, *J. Geophys. Res.* **57**, 227-286 (1952).

5.      H. K. Mao, G. Shen, R. J. Hemley, *Science* **278**, 2098-2100 (1997).

6.      T. Lay, Q. Williams, E. J. Garnero, *Nature* **392**, 461-468 (1998).

7.      D. P. Dobson, J. P. Brodholt, *Nature* **434**, 371-374 (2005).

8.      M. Murakami, K. Hirose, K. Kawamura, N. Sata, Y. Ohishi, *Science* **304**, 855-858 (2004).

9.      A. R. Oganov, S. Ono, *Nature* **430**, 445-448 (2004).

10.     S.-H. Shim, T. S. Duffy, R. Jeanloz, G. Shen, *Geophys. Res. Lett.* **DOI:10.1029** (2004).

11.     T. Iitaka, K. Hirose, K. Kawamura, M. Murakami, *Nature* **430**, 442-445 (2004).

12.     W. L. Mao *et al.*, *Proc. Nat. Aca. Sci.* **101**, 15867-15869 (2004).

13.     C. S. Zha, W. A. Bassett, S. H. Shim, *Rev. Sci. Instru.* **75**, 2409-2418 (2004).

14.     A. P. Hammersley, *ESRF internal report* **ESRF97HA02T** (1997).

15.     J. P. Perdew, K. Burke, M. Ernzerhof, *Phys. Rev. Lett.* **77**, 3865-3868 (1996).

16.     P. Hohenberg, W. Kohn, *Phys. Rev.* **136**, B864-B871 (1964).

17.     W. Kohn, L. J. Sham, *Phys. Rev.* **140**, A1133-A1138 (1965).

18.     X. Gonze *et al.*, *Comp. Mater. Science* **25**, 478-492 (2002).

19.     M. Fuchs, M. Scheffler, *Comput. Phys. Commun.* **119**, 67-98 (1999).

20.     H. J. Monkhorst, J. D. Pack, *Phys. Rev. B* **13**, 5188-5192 (1976).

21.     T. Yagi, H. K. Mao, P. M. Bell, *Carnegie Inst. Washington Yearb.* **77**, 837-841 (1978).

22.     J. Badro *et al.*, *Science* **305**, 383-385 (2004).

23. R. E. Cohen, I. I. Mazin, D. E. Isaak, *Science* **275**, 654-657 (1997).

24. J. Li *et al.*, *Proc. Nat. Acad. Sci.* **101**, 14027-14030 (2004).

25. D. L. Anderson, in *The EDGES of the mantle* M. Gurnis, M. E. Wysession, E. Knittle, B. A. Buffett, Eds. (American Geophysical Union, Washington, D.C., 1998) pp. 255-271.

26. I. Sidorin, M. Gurnis, D. V. Helmberger, *Science* **286**, 1326-1331 (1999).

27. T. Nakagawa, P. J. Tackley, *Geophy. Res. Lett.* **31**, L16611-4 (2004).

28. L. Wen, D. V. Helmberger, *Science* **279**, 1701-1703 (1998).

29. E. J. Garnero, *Science* **304**, 834-836 (2004).

30. T. S. Duffy, *Nature* **430**, 409-410 (2004).

31. J. C. Jamieson, J. N. Fritz, M. H. Manghanani, in *High Pressure Research in Geophysics* S. Akimoto, M. H. Manghanani, Eds. (Center for Academic Publications, Boston, 1982), vol. 12, pp. 27-48.

32. T. Tsuchiya, J. Tsuchiya, K. Umemoto, R. M. Wentzcovitch, *Geophy. Res. Lett.* **31**, L14603 (2004).

33. M. Murakami, K. Hirose, S. Ono, *Geophys. Res. Lett.* **30**, 1207-1210 (2003).

**Table 1**. Pressures, Miller indices, and lattice parameters for ppv-phase Fs20, Fs40, Fs60, and Fs80.

| | Fs20, 147 GPa | | Fs40, 141 GPa | | Fs60, 124 GPa | | Fs80, 142 GPa | |
|---|---|---|---|---|---|---|---|---|
| $a$ (Å) | 2.458(2) | | 2.463(3) | | 2.475(3) | | 2.463(2) | |
| $b$ (Å) | 8.064(5) | | 8.047(8) | | 8.183(7) | | 8.111(9) | |
| $c$ (Å) | 6.104(2) | | 6.115(3) | | 6.159(3) | | 6.113(2) | |
| $V$ (Å$^3$) | 121.0(1) | | 121.2(2) | | 124.7(2) | | 122.1(2) | |
| hkl | d-spacing (Å) | | d-spacing (Å) | | d-spacing (Å) | | d-spacing (Å) | |
| | Observed | Calculated | Observed | Calculated | Observed | Calculated | Observed | Calculated |
| 020 | 4.034 | 4.032 | - | - | - | - | - | - |
| 022 | 2.443 | 2.444 | 2.437 | 2.434 | 2.460 | 2.460 | 2.444 | 2.441 |
| 110 | 2.351 | 2.352 | - | - | - | - | - | - |
| 023 | 1.815 | 1.817 | 1.816 | 1.818 | 1.834 | 1.835 | 1.820 | 1.821 |
| 131 | 1.739 | 1.739 | 1.740 | 1.739 | 1.759 | 1.757 | 1.744 | 1.745 |
| 132 | 1.560 | 1.559 | 1.561 | 1.560 | 1.576 | 1.575 | 1.565 | 1.564 |
| 113 | 1.539 | 1.539 | 1.542 | 1.541 | 1.551 | 1.551 | 1.542 | 1.541 |
| 004 | 1.525 | 1.526 | 1.528 | 1.529 | 1.539 | 1.540 | 1.528 | 1.528 |
| 062* | 1.239 | 1.239 | 1.232 | 1.23 | 1.247 | 1.248 | - | - |
| 044 | 1.217 | 1.217 | 1.218 | 1.217 | 1.231 | 1.230 | - | - |

*the 062 peak contains contributions from the 152, 062, and 200 reflections.

**Figure Captions**

**Fig. 1**. X-ray diffraction patterns for a) Fs20 at 147 GPa ($\lambda$ = 0.3888 Å); b) Fs40 at 141 GPa ($\lambda$ = 0.4233 Å), Fs60 at 124 GPa ($\lambda$ = 0.4008 Å), and Fs80 at 138 GPa ($\lambda$ = 0.4057 Å). ppv peaks are additionally marked with *. Re oxide peaks are marked with †. Pressures were determined from the EOS of Pt (*31*). The crystal structure of ppv is shown on the right where silicon octahedral are shown in blue and iron and magnesium cations are shown in yellow.

**Fig. 2**. Enthalpy of ppv compared to the silicate perovskite phase of the same composition (the zero horizontal line) with respect to pressure in the $MgSiO_3$-$FeSiO_3$ system.

**Fig. 3**. Density and relative volume of the ppv phase as a function of *x*. For comparison, results are corrected to the same pressure at 130 GPa using the theoretical bulk modulus and elastic constants (*11, 32*). Volume is normalized to Fs20 ($V/V_{Fs20}$). Density is shown with comparison to Fs12 silicate perovskite (X symbol shown with 1% error bar) and the $\alpha$-$PbO_2$-type (dotted line) and $CaCl_2$-type (dashed line) $SiO_2$ phases (*33*).

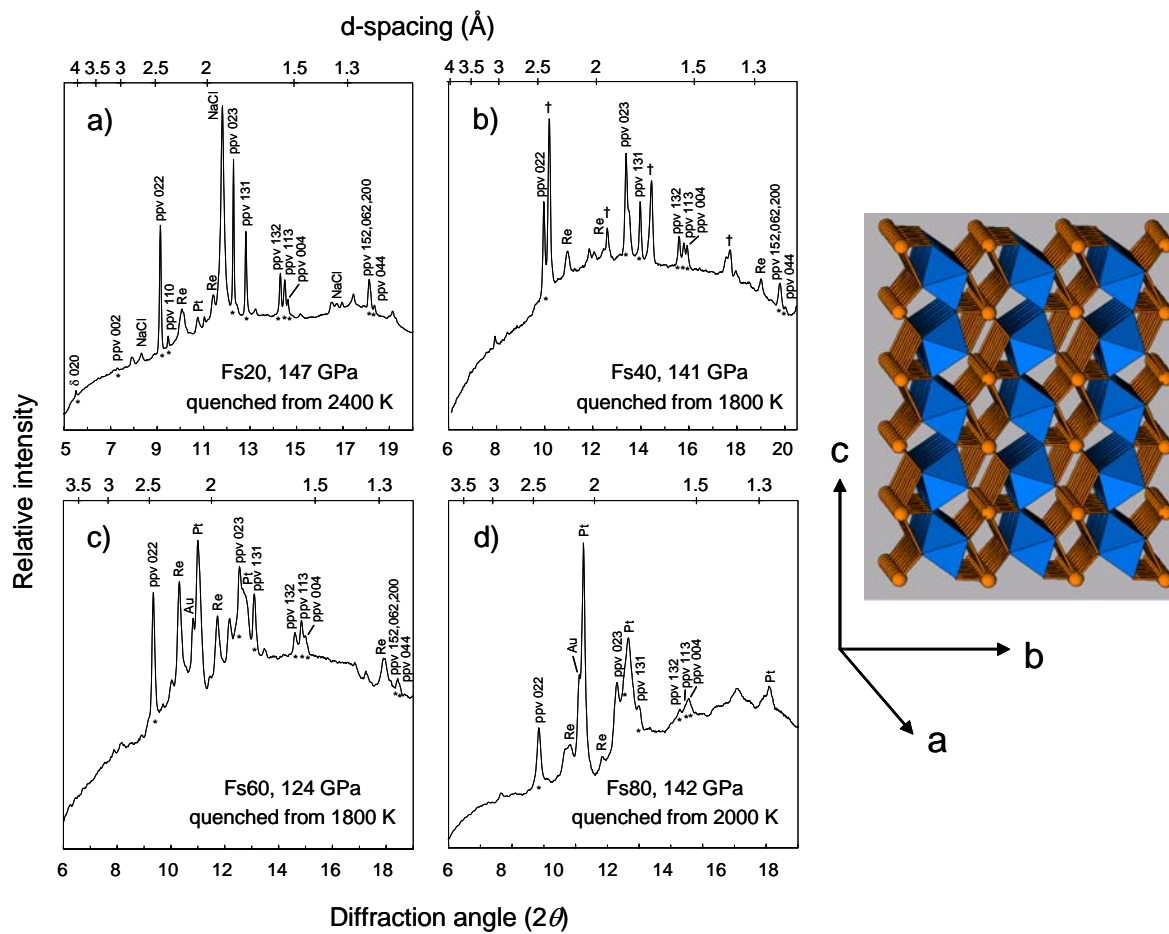**Fig. 4**. Schematic diagram of the reaction boundary between an iron-poor mantle and iron-rich core and the accumulation of iron-rich ppv in LVZ and ULVZ.
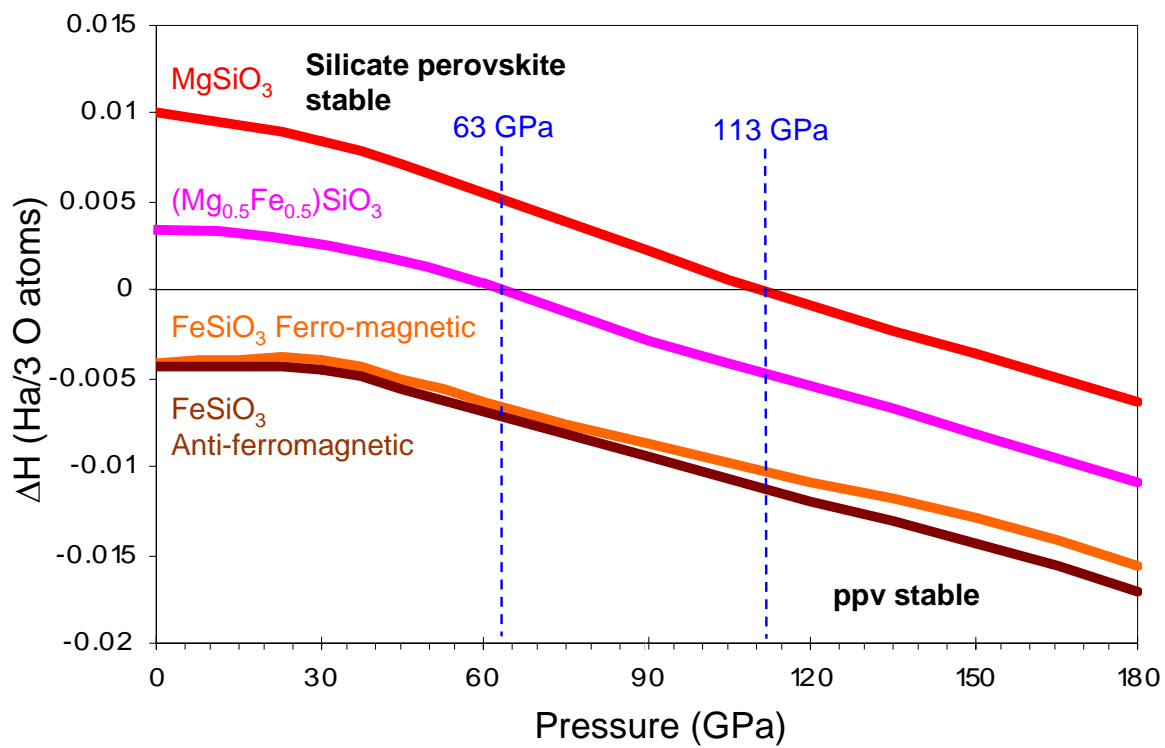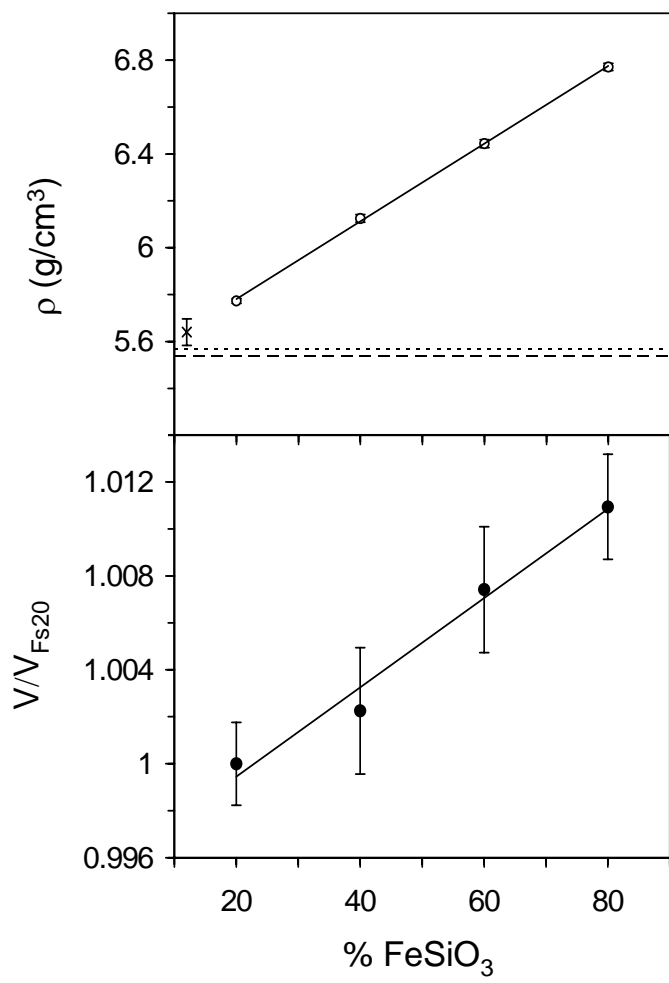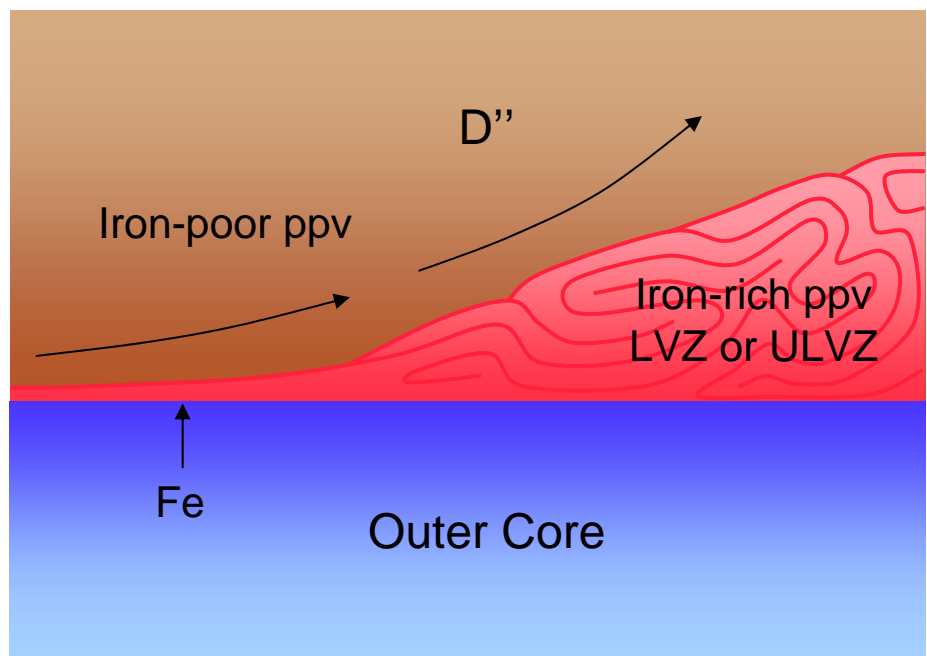
Fig. 1

Fig. 2

Fig. 3

Fig. 4